



Article

Prediction of Shearing and Ploughing Constants in Milling of Inconel 718

Chi-Jen Lin ¹, Yu-Ting Lui ², Yu-Fu Lin ², Hsian-Bing Wang ², Steven Y. Liang ³ and Jiunn-Jyh Junz Wang ^{1,*}

¹ Department of Mechanical Engineering, National Cheng Kung University, Tainan 701, Taiwan; lin831220@gmail.com

² Metal Industries Research & Development Center, Kaohsiung 811, Taiwan; lyting@mail.mirdc.org.tw (Y.-T.L.); yufulin@mail.mirdc.org.tw (Y.-F.L.); pk0148697@mail.mirdc.org.tw (H.-B.W.)

³ George W. Woodruff School of Mechanical Engineering, Georgia Institute of Technology, Atlanta, GA 30332, USA; steven.liang@me.gatech.edu

* Correspondence: jjwang@mail.ncku.edu.tw

Abstract: The present study proposes an integrated prediction model for both shearing and ploughing constants for the peripheral milling of Inconel 718 by using a preidentified mean normal friction coefficient. An equation is presented for the identification of normal mean friction angle of oblique cutting in milling. A simplified oblique cutting model is adopted for obtaining the shear strain and shearing constants for a tool of given helix angle, radial rake angle, and honed edge radius. The shearing and ploughing constants predicted from analytical model using the Merchant's shear angle formula and the shear flow stress from the selected Johnson–Cook material law are shown to be consistent with the experimental results. The experimentally identified normal friction angles and shearing and edge ploughing constants for the Inconel 718 milling process are demonstrated to have approximately constant values irrespective of the average chip thickness. Moreover, the predicted forces obtained in milling aged Inconel 718 alloy are in good agreement with the experimental force measurements reported in the literature. Without considering the thermal–mechanical coupling effect in the material law, the presented model is demonstrated to work well for milling of both annealed and aged Inconel 718.

Keywords: milling; friction coefficient; shearing constants; ploughing constants; Inconel 718



Citation: Lin, C.-J.; Lui, Y.-T.; Lin, Y.-F.; Wang, H.-B.; Liang, S.Y.; Wang, J.J. Prediction of Shearing and Ploughing Constants in Milling of Inconel 718. *J. Manuf. Mater. Process.* **2021**, *5*, 8. <https://doi.org/10.3390/jmmp5010008>

Received: 9 December 2020

Accepted: 6 January 2021

Published: 11 January 2021

Publisher's Note: MDPI stays neutral with regard to jurisdictional claims in published maps and institutional affiliations.



Copyright: © 2021 by the authors. Licensee MDPI, Basel, Switzerland. This article is an open access article distributed under the terms and conditions of the Creative Commons Attribution (CC BY) license (<https://creativecommons.org/licenses/by/4.0/>).

1. Introduction

The milling process is widely used throughout manufacturing industry for the forming and finishing of mechanical parts and components. Among the parameters involved in the milling process, cutting force is one of the most critical factors affecting the tool wear, surface roughness, and residual stress of the machined component. Therefore, an analytical milling force model can be employed to predict the quality of finished parts and implement process optimization strategies.

Milling force comprises the local single-point cutting forces on the multi-fluted cutting edges. In the single-point cutting force model, Merchant [1], Palmer and Oxley [2], and Armarego and Brown [3] established the relationship of cutting force components in the primary and secondary shear planes, as well as the shear angle prediction method, in the orthogonal and oblique cutting mechanism. Stabler [4] indicated that, under oblique cutting, the chip flow angle is approximately the same as the normal rake angle and is independent of the cutting speed and rake angle. However, these theories did not consider the effect of the honed cutting edge. Kobayashi and Thomsen [5] proposed that an edge ploughing force exists in addition to the shearing force during cutting. Albrecht [6] demonstrated that the ploughing mechanism at the edge of the cutting tool produced an additional cutting force. Waldorf et al. [7] developed a slip-line field model for predicting the ploughing force during orthogonal cutting. The results indicated that the ploughing

force increased as the tool edge radius increased, but was unaffected by the feed rate during turning. In a later study [8], Waldorf simplified the ploughing force model on the basis of the shear stress of the shear plane, edge radius, rake angle, and cutting width.

The edge ploughing effect becomes more dominant than the chip shearing effect as the uncut chip thickness is comparable in size to the edge radius as in micromachining and is important in examining the material removal mechanisms, cutting forces, and surface generation. The minimum chip thickness, below which material is not removed, and the ploughing force model for the elastic and plastic deformation near and under the cutting edge have been the subjects of many studies in micromilling [9–13] and in ultraprecision machining [14,15]. Malekian et al. [10] considered the minimum chip thickness to be approximately 0.3 of the edge radius for aluminum. Rahman et al. [14] presented a regression model for the optimum range of uncut chip thickness-to-edge radius ratio, defined as the relative tool sharpness (RTS), for the best finished surface as a function of material hardness. It was shown that a harder material led to a smaller value of critical RTS. The optimum range was found to be from 0.2 to 0.7 for the harder material of medium-carbon steel to the softer magnesium alloy, respectively. Rahmann et al. [15] further presented an equation of the specific cutting energy in extrusion-like cutting mechanism with the influence of the cutting-edge effect. The drastic increase in cutting energy was shown to correlate with a change from shearing to extrusion-like mechanism leading to the formation of a superior quality surface through the compressive material flow. The minimum chip thickness effect and the extrusion-like mechanism are not considered in the macromilling process presented in this paper since the average chip thickness, ranging from 22 μm to 33 μm , is much greater than the edge radius of 3 to 10 μm for the helical end mill in use.

In the milling force model, Koenigsberger and Sabberwal [16] proposed that the tangential force is a function of the undeformed chip thickness, and they developed the concept of specific cutting coefficients. Kline et al. [17] used the tangential and radial cutting coefficients to establish a two-dimensional (2D) end milling force model, establishing said coefficients as functions of the average chip thickness. The two coefficients, calculated from the average chip thickness of given process parameters, are treated as constants when calculating the local cutting force with respect to the varying chip thickness. The cutting coefficients in the aforementioned model represent the lumped effects of the shearing and ploughing mechanisms, and this was defined as the lumped global cutting constant (LGCC) model by Wang and Zheng [18]. Thus, the lumped cutting coefficients are constants with respect to the varying local chip thickness. In [18], the dual-mechanism counterpart of LGCC was defined as the dual-mechanism global cutting constant (DGCC), where the shearing and ploughing cutting coefficients are separately considered, assumed to be independent of the varying chip thickness and, thus, referred to as cutting constants. Yellowley [19] presented the first DGCC 2D milling force model, which assumed that both the shearing coefficient and the ploughing coefficient are constant.

Under these local cutting force models, total milling force models are usually constructed using numerical integration. Wang et al. [20] obtained the 2D total milling forces through the convolution integral of an LGCC local force model. Zheng et al. [21] presented a three-dimensional convolution model for cutting forces in peripheral end milling on the basis of lumped cutting constants, cutting parameters, machining configuration, and tool/work geometry. Wang and Zheng [18] extended the convolution approach to establish a three-axis DGCC force model for end milling. In these time-domain convolution models, Fourier coefficients of the periodic milling forces can be analytically obtained through Fourier transform and expressed in terms of LGCCs or DGCCs. Furthermore, the three mechanistic LGCCs could be inversely identified from the average forces of one milling experiment [21], and the six mechanistic DGCCs could be identified from six average force components of two milling experiments with different average chip thicknesses [18]. These chip-thickness-independent mechanistic cutting constants facilitate the computation of local and total cutting forces for milling cutters with complex geometry; however, experi-

mentation is required for the given tool–work material to identify their in-situ values under specified cutting conditions. Wojciechowski et al. [22] presented a mechanistic edge force coefficient model as a function of surface inclination angle and tool flank wear for accurate force prediction of finish ball end milling of an inclined surface.

Armarego and Whitfield [23] proposed a three-dimensional chip-thickness-dependent dual-mechanism variable cutting coefficient (DVCC) force model with three shearing and three ploughing coefficients for commonly executed machining operations, namely, turning, drilling, and milling. On the basis of oblique cutting mechanics described in [3], Budak et al. [24] established a DVCC model with six cutting coefficients by using basic cutting data such as shear angle and shear stress data that were obtained from orthogonal cutting experiments. Armarego and Whitfield [23] and Budak et al. [24] derived the three ploughing coefficients separately through orthogonal cutting experiments. Their DVCC models can be classified as semi-analytical models because constructing a cutting database would require machining experimentation. Gonzalo et al. [25] used the finite element method as a substitute for orthogonal cutting experiments in predicting cutting coefficients.

DVCC models can be considered analytical models if the material flow stress in the primary shear plane can be predicted using a material flow stress constitutive model. To model helical end milling forces, Li et al. [26] predicted side cutting edge, end cutting edge, and nose radius effects by using oblique machining theory along with work material flow stress properties. On the basis of the Johnson–Cook material model proposed by Kobayashi et al. [27], Li and Wang [28] presented a force model for the milling of Inconel 718. Moreover, Moufki et al. [29] employed a thermomechanical model of oblique cutting and the Johnson–Cook model proposed by Uhlmann et al. [30] to predict the three shearing coefficients for Inconel 718 along with the three experimental ploughing constants for peripheral milling processes. Lu et al. [31] executed a coupled thermomechanical analysis of the micromilling of Inconel 718 to predict cutting forces and temperatures; both shearing and ploughing forces were predicted using oblique cutting theory, with the effective edge radius being a function of chip thickness. Long et al. [32] used Merchant’s law and the Johnson–Cook model in [30] to predict the shear angle and shear flow stress, respectively, and applied the slip-line field model developed by Waldorf et al. [7] to predict ploughing forces. Ozel et al. [33] modified the Johnson–Cook (J–C) model presented by Lorentzon et al. [34] for Inconel 718 by incorporating the flow softening phenomenon through finite element simulations; they validated the simulations by using experimental data derived from face turning as a benchmark. Pawade et al. [35] presented an analytical model to predict the specific shear energy in turning of Inconel 718 using J–C model from Ahmed et al. [36]. The specific shear energy was shown to vary by as much as three times for the same tool edge geometry under the same cutting speed at different depths of cut and feeds. Using the J–C model, Sonawane and Joshi [37] predicted the variable cutting coefficients for ball end milling of Inconel 718. The shear angle is predicted according to the tool space and volume constancy as a function of cutter rotation angle, instantaneous cutter radius, cutter helix angle, and cutting parameters.

As mentioned, for milling processes, studies have derived shearing and ploughing constants or coefficients either directly through milling experiments by using mechanistic DGCC models [16–21] or indirectly through machining data for tool–work material combinations by using semi analytical DVCC models [23,24]. Analytical DVCC models [26,27,29,31] predict shearing and ploughing forces and coefficients without costly experimentation and can be applied to an extensive range of tools with complex micro and macro geometrical structures. However, they require a relatively complex thermomechanical model of oblique cutting along with a suitable work material flow stress model and a rake face normal friction coefficient. Akmal et al. [38] provided a direct approach for determining the friction coefficient, β_n , from slot milling of Ti6Al4V using orthogonal cutting theory. The friction angle at the rake face of an orthogonal cutting is related to the normal friction angle by $\tan\beta_n = \tan\beta_a \cos\eta_c$, where the chip flow angle, η_c , is difficult to measure in a milling process and can be predicted using oblique cutting theory.

To facilitate the practical application of oblique cutting mechanics in an industrial setting, the present study presents a DGCC prediction model for the milling of hard-to-machine Inconel 718; the proposed model integrates the advantages of mechanistic DGCC models and analytical DVCC models. Accordingly, the present study proposes an integrated prediction model for both shearing and ploughing constants for the peripheral milling of Inconel 718 by using a preidentified mean normal friction coefficient and a simplified oblique cutting model. The remainder of this paper is organized as follows: in Section 2, equations for the six DGCCs are first derived by integrating orthogonal cutting theory with Waldorf’s edge ploughing force model and oblique cutting theory along with the Johnson–Cook constitutive equation. Section 3 then presents the derivation of the six mechanistic cutting constants for peripheral milling and friction angle from experimental data, followed by experimental verification in Section 4 and conclusions in Section 5.

2. Predicting Shear and Ploughing Constants of Peripheral Milling

Figure 1 presents a schematic representation of the peripheral milling process in the X–Y–Z work coordinate system, where f_t is the local tangential cutting force and f_r is the radial force with instantaneous chip thickness, t_c . θ_1 and θ_2 are the entry and exit angles, respectively. a_e and a_p are the radial and axial depths of cut, respectively. The shear and ploughing cutting constants for orthogonal cutting are first derived, followed by presenting the formula for DGCCs associated with the helical cutting edge of given radial rake and edge radius.

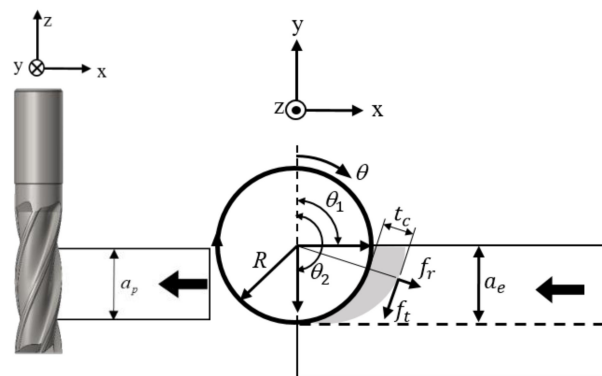


Figure 1. Schematic representation of the peripheral milling process.

2.1. Shear Constants of Orthogonal Cutting

According to Merchant [1], the geometric relationship among the cutting forces produced in orthogonal cutting has the form depicted in Figure 2.

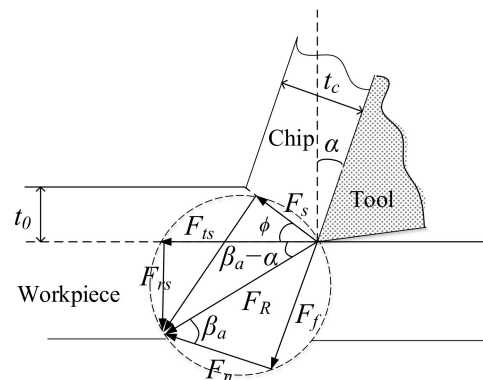


Figure 2. Force components in Merchant circle [1].

Moreover, the rake angle, α , friction angle, β , and shear angle, ϕ , are assumed to be related by Merchant’s law as follows [39]:

$$\phi = \frac{\pi}{4} - \frac{\beta}{2} + \frac{\alpha}{2} \tag{1}$$

where β is the mean friction angle on the rake face with the mean friction coefficient, μ , as

$$\mu = \tan \beta \tag{2}$$

The effective strain along the shear plane can be calculated as follows [40]:

$$\varepsilon = \frac{\gamma}{\sqrt{3}}, \gamma = \frac{\cos \alpha}{\sin \phi \cdot \cos(\phi - \alpha)} \tag{3}$$

Meanwhile, the strain rate on the shear plane can be obtained as

$$\dot{\varepsilon} = \frac{\dot{\gamma}}{\sqrt{3}}, \dot{\gamma} = \frac{\cos \alpha}{\cos(\phi - \alpha)} \cdot \frac{V_c}{\Delta y} \tag{4}$$

where V_c is the tangential cutting velocity, and Δy is the average shear band thickness (~25 μm) [41]. The shear flow stress on the shear plane can be obtained from the material constitutive equation proposed by Johnson and Cook [42] as

$$\tau = \frac{\sigma}{\sqrt{3}}, \sigma = (A + B\varepsilon^n)(1 + C \ln \frac{\dot{\varepsilon}}{\dot{\varepsilon}_0})(1 - (\frac{T - T_{room}}{T_{melt} - T_{room}})^m) \tag{5}$$

where τ is the shear flow stress, σ is the flow stress, ε is the effective strain, $\dot{\varepsilon}$ is the strain rate, $\dot{\varepsilon}_0$ is the reference strain rate, T is the workpiece initial temperature, T_{room} is room temperature, and T_{melt} is the melting point of the material. In addition, A, B, C, m , and n are material parameters with values determined from split Hopkinson pressure bar (SHPB) experiments performed at known work material temperatures and strain rates. In the present study, the J–C parameters used by Lorentzon et al. [34] are used to model the Inconel 718 under high-strain-rate deformation conditions. The relevant parameters and values of the model are listed in Table 1.

Table 1. Johnson–Cook parameters for aged Inconel 718 [34].

| A (MPa) | B (MPa) | C | n | m | $\dot{\varepsilon}_0$ (1/s) | T_{melt} (K) |
|---------|---------|--------|--------|-----|-----------------------------|----------------|
| 1241 | 622 | 0.0134 | 0.6522 | 1.3 | 1 | 1573 |

The shear flow stress, τ , on the shear plane and the cutting or tangential force, F_c , in Figure 2, are related as

$$F_{ts} = \frac{t_0 \cdot w \cdot \tau \cdot \cos(\beta - \alpha)}{\sin \phi \cdot \cos(\phi + \beta - \alpha)} \tag{6}$$

where t_0 is the uncut chip thickness, and w is the cutting width. Meanwhile, the tangential shearing constant K_{ts_or} and radial shearing constant k_{rs_or} of orthogonal cutting can be expressed, respectively, as

$$K_{ts_or} = \frac{F_{ts}}{t_0 \cdot w} = \frac{\tau \cdot \cos(\beta - \alpha)}{\sin \phi \cdot \cos(\phi + \beta - \alpha)} \tag{7}$$

$$k_{rs_or} = \frac{F_{rs}}{F_t} = \tan(\beta - \alpha) \tag{8}$$

2.2. Tool Edge Ploughing Constants of Orthogonal Cutting

Orthogonal cutting theory [1] assumes that the cutting tool edge has an ideal sharp geometry. However, in practice, the cutting tool edge has a finite honed radius. Consequently, a tool edge ploughing effect is produced, as illustrated in Figure 3. In the present study, the ploughing effect is described using the simplified slip-line field model proposed by Waldorf [8].

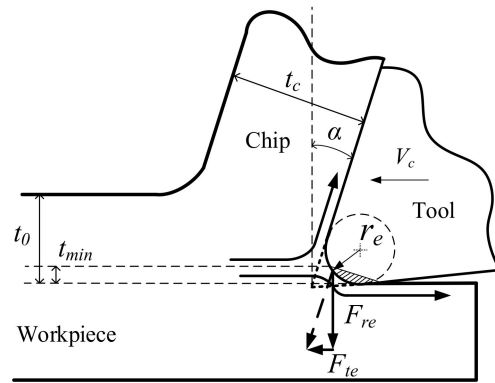


Figure 3. Tool edge ploughing mechanism of orthogonal cutting.

In particular, the tangential ploughing force, F_{ce} , and axial ploughing force, F_{te} , are expressed, respectively, as

$$\begin{aligned} F_{te} &= \tau \cdot w \cdot r_e \cdot \tan\left(\frac{\pi}{4} + \frac{\alpha}{2}\right) \\ F_{re} &= F_{te}\left(1 + \frac{\pi}{2}\right) \end{aligned} \tag{9}$$

where τ is the shear stress on the shear plane, w is the cutting width, r_e is the tool edge radius, and α is the rake angle. This ploughing force is attributed to a combination of the chip forming force for material above the t_{min} , the minimum uncut chip thickness, and the rubbing or ploughing force generated by the shaded interference area for material below the t_{min} line shown in Figure 3. The tangential ploughing coefficient, K_{te_or} , and radial ploughing coefficient, k_{re_or} , of orthogonal cutting are then given, respectively, as

$$K_{te_or} = \frac{F_{te}}{w} = \tau \cdot r_e \cdot \tan\left(\frac{\pi}{4} + \frac{\alpha}{2}\right) \tag{10}$$

$$k_{re_or} = \frac{F_{re}}{F_{te}} = 1 + \frac{\pi}{2} \tag{11}$$

2.3. Six Shearing and Ploughing Constants of Oblique Cutting in DGCC Milling Model

In contrast to the orthogonal cutting mode, in which the cutting force has just two dimensions, oblique cutting results in a three-dimensional cutting force due to the effect of the helix angle i . Referring to Figure 4, the normal rake angle, α_n , radial rake angle, α_r , and inclination angle, i , are related as follows [3]:

$$\tan \alpha_n = \tan \alpha_r \cdot \cos i \tag{12}$$

The inclination angle corresponds to the helix angle of a helical end mill in the milling process. Using the geometric relationship between orthogonal and oblique cutting derived by Armarego and Brown [3] and the Stabler rule [4], Gonzalo et al. [25] showed that the chip flow angle has a value of $\eta_c \approx i$ in oblique milling. With the assumption of $\eta_c = i$, referring to the three shear coefficient formulas of Budak et al. [24] for oblique cutting, the

radial and axial directions are converted to ratios and the dual-mechanism global cutting constant (DGCC) model, thus, has the following three shearing constants:

$$\begin{aligned}
 K_{ts} &= \frac{\tau}{\sin \phi_n} \cdot \frac{\cos(\beta_n - \alpha_n) + \sin \beta_n \cdot \tan^2 i}{\sqrt{\cos^2(\phi_n + \beta_n - \alpha_n) + \tan^2 i \cdot \sin^2 \beta_n}} \\
 k_{rs} &= \frac{\sin(\beta_n - \alpha_n)}{\cos i \cdot (\cos(\beta_n - \alpha_n) + \sin \beta_n \cdot \tan^2 i)} \\
 k_{as} &= \frac{\cos(\beta_n - \alpha_n) \cdot \tan i - \tan i \cdot \sin \beta_n}{\cos(\beta_n - \alpha_n) + \sin \beta_n \cdot \tan^2 i}
 \end{aligned}
 \tag{13}$$

where K_{ts} (MPa or N/mm²) is the tangential shearing constant or specific shearing energy, k_{rs} is the ratio of the radial and tangential shearing constants, and k_{as} is the ratio of the axial and tangential shearing constants. In transforming orthogonal cutting to oblique cutting in Equation (13), the chip flow angle is taken to be the same as the inclination angle, and the normal shear angle, θ_n , the normal mean friction angle, β_n , and shear flow stress, τ , are assumed to be the same as those obtained in orthogonal cutting. These assumptions were applied as practical approaches in predicting oblique cutting force from the orthogonal cutting database [43]. These three shear constants are further assumed to be independent of the varying chip thickness in the peripheral milling process.

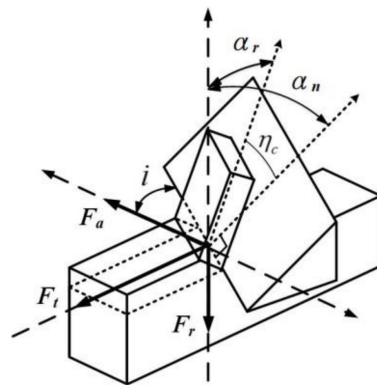


Figure 4. Oblique cutting geometry.

Among the many variables in Equation (13), only i and α_n are known for a given helical tool, with the remaining unknowns being the normal mean friction angle, β_n , normal shear angle, ϕ_n , and shear flow stress, τ . This paper proposes identifying the normal mean friction angle from the experimental k_{rs} value, the expression of which in Equation (13) has only one unknown, β_n . The normal shear angle and shear flow stress can then be calculated using Equations (1)–(5).

Since the cutting direction and magnitude of the ploughing force are hardly affected by orthogonal and oblique cutting mechanisms, k_{ae} is set to zero [23] and the ploughing constants of oblique cutting are the same as those of orthogonal cutting. That is,

$$\begin{aligned}
 K_{te} &= K_{te_{or}} = \tau \cdot r_e \cdot \tan\left(\frac{\pi}{4} + \frac{\alpha_n}{2}\right) \\
 k_{re} &= \frac{K_{re}}{K_{te}} = k_{re_{or}} = 1 + \frac{\pi}{2}
 \end{aligned}
 \tag{14}$$

where the shear flow stress, τ , has the same value as that in Equation (13) for the shearing mechanism.

3. Identifying DGCC Constants and Friction Angle from Experimental Data

3.1. Experimental Determination of DGCC Milling Constants

The predicted milling constants were validated against constants experimentally obtained from the DGCC model proposed in [18] using Inconel 718 alloy as the work-piece material.

In the DGCC model, the shearing and ploughing constants can be estimated inversely from two experimental force measurements obtained under two different feeds per tooth, δ_1 and δ_2 , at the same axial depth of cut, a_p , and radial depth of cut, a_e .

$$\begin{bmatrix} K_{ts} \\ K_{ts}k_{rs} \\ K_{ts}k_{as} \\ K_{te} \\ K_{te}k_{re} \\ K_{te}k_{ae} \end{bmatrix} = \frac{2\pi}{N \cdot a_p} T^{-1} \begin{bmatrix} A_{sx1} \\ A_{sy1} \\ A_{sz1} \\ A_{sx2} \\ A_{sy2} \\ A_{sz2} \end{bmatrix} \tag{15}$$

where N is the number of flutes, and T is transformation matrix with

$$T = \begin{bmatrix} P_1\delta_1 & -P_2\delta_1 & 0 & P_4 & -P_5 & 0 \\ P_2\delta_1 & P_1\delta_1 & 0 & P_5 & P_4 & 0 \\ 0 & 0 & -P_3\delta_1 & 0 & 0 & -P_6 \\ P_1\delta_2 & -P_2\delta_2 & 0 & P_4 & -P_5 & 0 \\ P_2\delta_2 & P_1\delta_2 & 0 & P_5 & P_4 & 0 \\ 0 & 0 & -P_3\delta_2 & 0 & 0 & -P_6 \end{bmatrix}$$

in which

$$\begin{aligned} P_1 &= 0.25(\cos 2\theta_1 - \cos 2\theta_2) \\ P_2 &= 0.5(\theta_2 - \theta_1) + 0.25(\sin 2\theta_1 - \sin 2\theta_2) \\ P_3 &= \cos \theta_2 - \cos \theta_1 \\ P_4 &= \sin \theta_2 - \sin \theta_1 \\ P_5 &= \cos \theta_2 - \cos \theta_1 \\ P_6 &= \theta_1 - \theta_2 \end{aligned}$$

where θ_1 and θ_2 are the entry and exit angles, respectively, for the given radial depth of cut, a_e . A_{sx} , A_{sy} , and A_{sz} are the measured average side edge milling force components in the X-, Y, and Z-directions, respectively, and indices 1 and 2 refer to the first and second experimental trials performed with smaller and larger radial depths of cut, respectively.

3.2. Removal of Bottom Tool Edge Ploughing Effect

For an end milling process, as the axial depth of cut reduces, the effect of the bottom tool edge ploughing mechanism increases and becomes a more significant part of the total force. Thus, to better explore the cutting constants of the side tool edge, it is desirable to isolate and remove the effect of the ploughing mechanism on the bottom edge. Through a similar approach presented in [38], the average milling force on the side edge of the cutter can be obtained from two sets of experiments performed at the same feed rate, but different axial cutting depths, a_p , in accordance with

$$\mathbf{A}_{s1} = \frac{(\mathbf{A}_2 - \mathbf{A}_1)}{a_{p2} - a_{p1}} \cdot a_{p1} \tag{16}$$

$$\mathbf{A}_{s2} = \frac{(\mathbf{A}_2 - \mathbf{A}_1)}{a_{p2} - a_{p1}} \cdot a_{p2} \tag{17}$$

$$\mathbf{A}_b = \mathbf{A}_1 - \mathbf{A}_{s1} = \mathbf{A}_2 - \mathbf{A}_{s2} \tag{18}$$

where \mathbf{A} is the total average force measured in the experiment, \mathbf{A}_s is the contribution of the side tool edge force to the total average force, and indices 1 and 2 refer to the first and second experiments performed with smaller and larger axial depths of cut, respectively.

3.3. Identifying Mean Friction Angle of Shear Mechanism

To predict the normal shear angle ϕ_n in oblique milling, approximated by ϕ from Equation (1), using Equation (1), it is first necessary to determine the average nominal

friction angle β_n between the chip and the tool face. Assuming that the tool geometry is known, the value of the friction angle can then be obtained using the ratio of the radial and tangential shearing constants k_{rs} , experimentally identified from Equation (15) by the following rearranged form of Equation (13):

$$\tan \beta_n = \frac{\sin \alpha_n + k_{rs} \cdot \cos i \cdot \cos \alpha_n}{\cos \alpha_n - k_{rs} \cdot \cos i \cdot (\sin \alpha_n + \tan^2 i)} \quad (19)$$

4. Results and Discussion

4.1. Prediction Model Verification Experiment

The validity of the cutting constants prediction model was verified by experiments performed using VDM Inconel 718 in annealed condition with a hardness of HBW 267 and a grain size of ASTM No. 6.5. The chemical composition of the VDM Inconel 718 is displayed in Table 2. As depicted in Figure 5a, the milling force during the milling process was measured using a dynamometer (Kistler Type-9272). The milling experiments were performed using RTA060052T two-blade tungsten carbide end mill coated with TiAlN. The hardness (HV_{30}) and rupture strength of the micro-grain carbide (90% WC, 10% Co, 0.6 μm grain size) were 1571 kg/mm^2 and 3750 N/mm^2 , respectively. The tool had a diameter of 6 mm, a helix angle of 35° , a radial rake angle of 14.9° , and a tool edge radius of 0.01 mm.

Table 2. Chemical composition of VDM Inconel 718 alloy (wt.%).

| Ni | Cr | C | Si | Mo | Co | Nb | Ta | Al | Ti | Cu | Fe |
|-------|-------|------|------|------|------|------|------|------|------|------|-------|
| 52.99 | 18.47 | 0.03 | 0.06 | 3.06 | 0.11 | 5.30 | 0.01 | 0.55 | 0.95 | 0.04 | 18.28 |

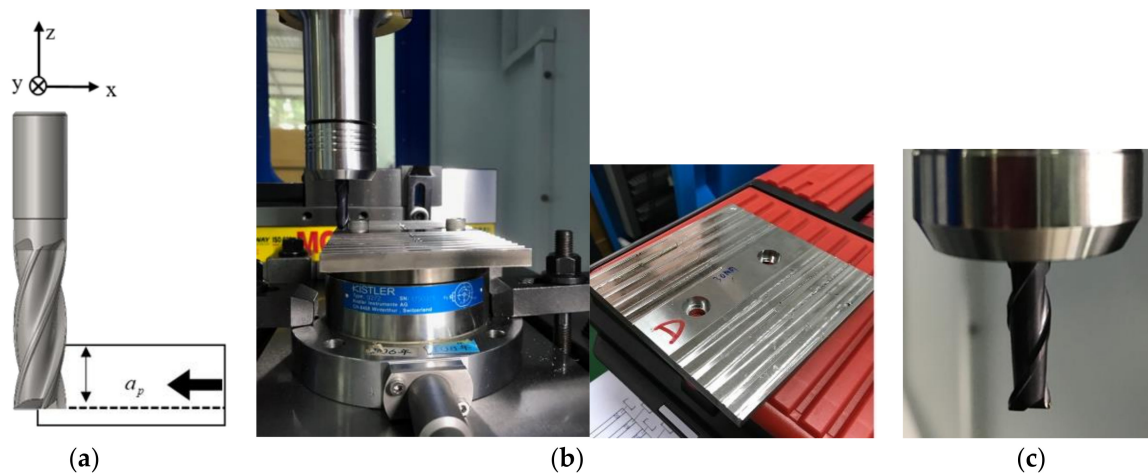


Figure 5. (a) Verification experiment setup; (b) Inconel 718 workpiece; (c) end mill.

To minimize the effects of tool wear on the accuracy of the experimental measurements, a new tool was used in each cutting experiment. The milling process was performed under dry conditions using the experimental parameters listed in Table 3. Since the aim of the proposed model was to predict the cutting constants of the side edge of the milling cutter as in a peripheral milling process, the effect of the bottom tool edge ploughing mechanism was eliminated by performing the experiments using two different axial cutting depths, (0.4, 0.6 mm) and (0.4, 0.5 mm), for the two radial depths at $a_e = 1.2$ and 1.5 mm, respectively.

Table 3. Verification experiment parameters.

| No. | S (rpm) | a_e (mm) | a_p (mm) | δ (mm/tooth) | \bar{t}_c (mm) |
|-----|----------------------------|------------|------------|---------------------|------------------|
| a1 | 3000 ($V_c = 56.5$ m/min) | 1.2 | 0.4 | 0.04 | 0.0172 |
| a2 | | | | 0.06 | 0.0259 |
| a3 | | | | 0.08 | 0.0345 |
| b1 | | 0.6 | 0.04 | 0.0172 | |
| b2 | | | 0.06 | 0.0259 | |
| b3 | | | 0.08 | 0.0345 | |
| c1 | | 1.5 | 0.4 | 0.04 | 0.0191 |
| c2 | | | | 0.06 | 0.0286 |
| c3 | | | | 0.08 | 0.0382 |
| d1 | 0.5 | 0.04 | 0.0191 | | |
| d2 | | 0.06 | 0.0286 | | |
| d3 | | 0.08 | 0.0382 | | |

Tables 4 and 5 show the total measured average forces \mathbf{A} , average side tool edge force \mathbf{A}_s , and average bottom tool edge force \mathbf{A}_b for experimental conditions **a** and **b**, and **c** and **d**, respectively.

Table 4. Total average force and average forces of side tool edge and bottom tool edge in experiments **a** and **b** with the radial depth of cut $a_e = 1.2$ mm.

| | | a1 | b1 | a2 | b2 | a3 | b3 |
|---------------------|----------|---------|---------|---------|---------|---------|---------|
| δ (mm/tooth) | | 0.04 | | 0.06 | | 0.08 | |
| a_p (mm) | | 0.4 | 0.6 | 0.4 | 0.6 | 0.4 | 0.6 |
| \mathbf{A} (N) | A_x | -5.297 | -7.020 | -7.355 | -10.278 | -9.498 | -13.542 |
| | A_y | -10.876 | -16.628 | -13.810 | -20.925 | -16.697 | -25.174 |
| | A_z | -6.078 | -4.740 | -4.378 | -2.401 | -4.934 | -2.399 |
| \mathbf{A}_s (N) | A_{sx} | -3.445 | -5.167 | -5.845 | -8.768 | -8.086 | -12.130 |
| | A_{sy} | -11.502 | -17.254 | -14.228 | -21.342 | -16.953 | -25.430 |
| | A_{sz} | 2.677 | 4.016 | 3.953 | 5.930 | 5.070 | 7.605 |
| \mathbf{A}_b (N) | A_{bx} | -1.852 | | -1.509 | | -1.412 | |
| | A_{by} | 0.626 | | 0.417 | | 0.255 | |
| | A_{bz} | -8.756 | | -8.332 | | -10.004 | |

Table 5. Total average force and average forces of side tool edge and bottom tool edge in experiments **c** and **d** with the radial depth of cut $a_e = 1.5$ mm.

| | | c1 | d1 | c2 | d2 | c3 | d3 |
|---------------------|----------|---------|---------|---------|---------|---------|---------|
| δ (mm/tooth) | | 0.04 | | 0.06 | | 0.08 | |
| a_p (mm) | | 0.4 | 0.5 | 0.4 | 0.5 | 0.4 | 0.5 |
| \mathbf{A} (N) | A_x | -6.343 | -7.598 | -8.877 | -10.889 | -11.628 | -14.298 |
| | A_y | -13.014 | -16.040 | -15.856 | -19.788 | -19.415 | -24.249 |
| | A_z | -3.567 | -2.677 | -3.973 | -2.648 | -3.662 | -2.128 |
| \mathbf{A}_s (N) | A_{sx} | -5.017 | -6.271 | -8.049 | -10.061 | -10.680 | -13.350 |
| | A_{sy} | -12.102 | -15.128 | -15.728 | -19.660 | -19.335 | -24.169 |
| | A_{sz} | 3.556 | 4.445 | 5.300 | 6.625 | 6.135 | 7.669 |
| \mathbf{A}_b (N) | A_{bx} | -1.326 | | -0.828 | | -0.948 | |
| | A_{by} | -0.911 | | -0.128 | | -0.079 | |
| | A_{bz} | -7.123 | | -9.273 | | -9.798 | |

4.2. Determination of Friction Coefficient

As stated above, for the experiments performed in the present study, the cutter had a helix angle, i , of 35° and a radial rake angle, α_r , of 14.9° . From Equation (13), the normal rake angle, α_n , was, thus, calculated to be 12.29° . The value of k_{rs} was obtained by substituting the average side tool edge forces given in Tables 4 and 5 under the same radial depths of cut and axial depths of cut but different feed rates into Equation (15). The normal mean friction angle, β_n , was then obtained from Equation (19) using the identified k_{rs} and known cutter geometry values. Finally, the friction coefficient was determined using Equation (2). Table 6 summarizes the results obtained from the friction angle analysis.

Table 6. Experimental mean friction angles.

| | | S (rpm) | 3000 | |
|----------------------------|------------|---|-------------------|-------------------|
| | | a_e (mm) | 1.2 | 1.5 |
| δ (mm/ tooth) | 0.04, 0.06 | \bar{f}_c (mm)/ k_{rs}/β_n (deg): | 0.022/0.243/25.94 | 0.024/0.190/22.81 |
| | 0.04, 0.08 | | 0.026/0.261/27.02 | 0.029/0.224/24.81 |
| | 0.06, 0.08 | | 0.030/0.279/28.11 | 0.033/0.260/26.96 |
| | | k_{rs_avg}/β_{n_avg} (deg)/ μ_{avg} : | 0.261/27.02/0.509 | 0.224/24.86/0.463 |
| | | k_{rs}/β_n (deg)/ μ : | 0.242/25.89/0.485 | |

As demonstrated in Table 6, the friction angles were relatively independent of the average chip thickness at both radial depths, although they did slightly increase with increasing average chip thickness. From the overall average k_{rs} value of 0.242, the normal mean friction angle over the two radial cutting depths at various feeds per tooth in the present experimental trials was found from Equation (19) to be $\beta_n = 25.89^\circ$ and the friction coefficient was 0.485. This mean friction angle of $\beta_n = 25.89^\circ$ was used for the analytical prediction of DGCC constants and milling force of Inconel 718 alloy.

4.3. Comparison of Predicted and Identified Cutting Constants

As presented in Table 6, the mean friction angle had an average value over the two radial cutting depths of $\beta_n = 25.89^\circ$. Moreover, as stated above, the tool had a normal rake angle of $\alpha_n = 12.29^\circ$. Thus, from Equation (1), the normal shear angle was obtained as $\phi_n = 38.26^\circ$. Given the known cutting speed of 3000 rpm, the shear strain, strain, and strain rate on the shear plane were determined to be $\gamma = 1.757$, $\varepsilon = 1.015$, and $\dot{\varepsilon} = 23,620 \text{ s}^{-1}$, respectively. Thus, from Equation (5), the flow stress and shear stress were equal to $\sigma = 2119 \text{ MPa}$ and $\tau = 1223 \text{ MPa}$, respectively, under room temperature conditions, $T = T_{room} = 298 \text{ K}$. From Equation (13), the oblique shearing constants in the DGCC model were found to be $K_{ts} = 3404 \text{ MPa}$, $k_{rs} = 0.242$, and $k_{as} = 0.316$, respectively. The tool had an edge radius of 0.01 mm. Hence, the edge ploughing constants were obtained from Equation (14) as $K_{te} = 15.2 \text{ N/mm}$, $k_{re} = 2.57$, and $k_{ae} = 0$, respectively.

Figure 6 compares the predicted values of the side tool edge cutting constants obtained using the DGCC model with the experimental values obtained for two different radial depths of cut (a_e). For the present case, the uncut chip thickness was generally greater than the tool edge radius. Consequently, the experimental results show that the values of K_{ts} , k_{rs} , and k_{as} did not vary significantly with the average chip thickness (\bar{t}_c). The analytical prediction for the three cutting constants showed a similar tendency. A good agreement was also observed between the experimental ploughing constants K_{te} and k_{re} and the analytical results.

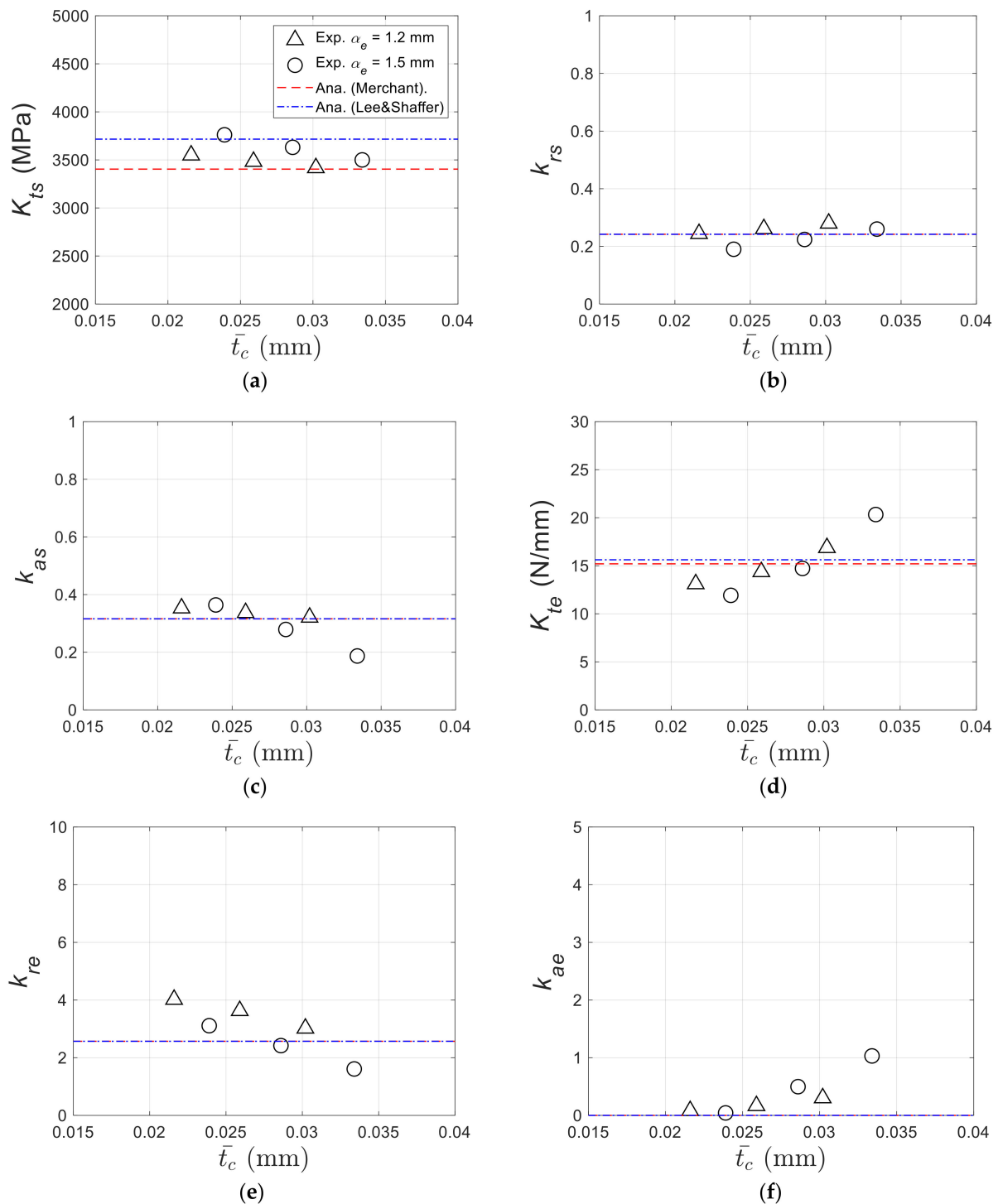


Figure 6. Comparison of experimental and predicted results for side tool edge cutting constants as a function of average chip thickness. Note that (a–c) show the shearing constants, while (d–f) show the edge ploughing constants.

From a detailed inspection, the predicted values of K_{ts} were found to deviate from the experimental results by no more than 10%. Similarly, most predicted values of k_{rs} deviated from the experimental results by no more than $\pm 14\%$, whereas most predicted values of k_{as} deviated from the experimental results by only $\pm 13.2\%$. The ploughing cutting constant values deviated more significantly from the experimental results in terms of percentage error because of their smaller absolute value. However, the ploughing force often accounted for a smaller proportion of the total cutting force and, hence, these errors had a small effect

on the prediction results obtained for the cutting force. As discussed in Section 2.2, the DGCC prediction model assumes that the direction and size of the ploughing effect are independent of the orthogonal or oblique cutting. As a result, the predicted value of k_{ae} is equal to zero [18]. However, the experimental results revealed that k_{ae} has a value of 0 to 1. This could be because of a difference in the axial force generated by the bottom edge at two different axial depths of cut, because the forces at the bottom were assumed to be the same regardless of their axial depths of cut in the analytical model. Variance in the bottom edge geometry of end mills might also have contributed to differences in bottom cutting and ploughing forces because a new tool was used for each experiment.

Notably, when the shear angle model proposed by Lee and Shaffer [44] was used ($\phi = \pi/4 - (\beta - \alpha)$), the shear angle was reduced to 31.4° , and shear strain and shear stress increased to 1.98 and 1258 MPa, respectively. The shearing constants then became $K_{ts_LS} = 3717$ MPa, $k_{rs} = 0.242$, and $k_{as} = 0.316$, and the edge ploughing constants were $K_{te_LS} = 15.62$ N/mm, $k_{re} = 2.57$, and $k_{ae} = 0$. Only the constants related to shear flow stress, namely, K_{ts} and k_{te} , were affected; they increased by 9.2% and 2.6%, respectively, compared with results using the shear angle from the Merchant model, but the radial force ratios were unchanged. The tangential shearing constants or the specific shearing energy, K_{ts_LS} , were demonstrated to lie on the upper bound of the experimental data in Figure 6a, whereas K_{ts} according to Merchant law was on the lower bound.

The main reason that the experimental shearing coefficients remain almost constant with respect to the average chip thickness is attributed to the fact that the ploughing force is separated from the total cutting force in the DGCC model and does not contribute to the specific shearing energy. If the shearing and ploughing forces are lumped together as in a LGCC model [21], the corresponding LGCC values can be shown to vary with chip thickness, as shown in Figure 7. The lumped tangential cutting constant, K_t , representing the average specific cutting energy of the milling process, is demonstrated to increase with decreasing average chip thickness, similar to the trend found in [15] for micromachining. The specific cutting energy in macromilling can be seen as the superposition of a constant specific shearing energy and an increasing specific apparent ploughing energy with decreasing chip thickness, which arises from a constant edge ploughing force divided by a decreasing uncut chip area. The specific cutting energy tends to converge to the shearing constant value of 3404 MPa in Figure 6 with increasing average chip thickness as the constant ploughing force becomes increasingly insignificant relative to the shearing force.

The average milling forces were predicted using the predicted DGCC values with $K_{ts} = 3404$ MPa. Figure 8 compares the experimental and predicted average forces and presents the percentage errors for experimental conditions. The errors are demonstrated to be within +21%/−23% of the experimental results. If $K_{ts_LS} = 3717$ MPa was used for force prediction, these errors would become 30%/−14%.

In addition to the choice of shear angle relationship, the selection of suitable material parameters among the many existing Johnson–Cook (J–C) constitutive laws in [33,45] for Inconel 718 also affects the predicted shear flow stress and cutting constants, which can differ by as much as 20% for the annealed 718 and 50% for the aged 718 at room temperature within a typical effective strain range of 1 to 1.5 in a machining application. These J–C parameters are mostly derived from SHPB tests with the maximum strains lower than 1, and with the maximum strain rates only reaching 3000 [27], 4600 [46,47], or 5000 [48] 1/s. When applied to machining process modeling, where effective strain and strain rate can exceed 1.5 and 30,000 1/s, respectively, prediction errors can be expected at these extrapolated ranges. For the presented experimental condition ($\epsilon = 1.014$ and $\dot{\epsilon} = 22,270$ s^{−1}) with an annealed 718 material, the J–C model for the annealed 718 from [47] and [30] would indicate a shear flow stress of approximately 1645 MPa; this is 34% higher than the 1225 MPa obtained from the model in [34] by Lorentzon et al., which was obtained from an SHPB test for an aged 718 material.

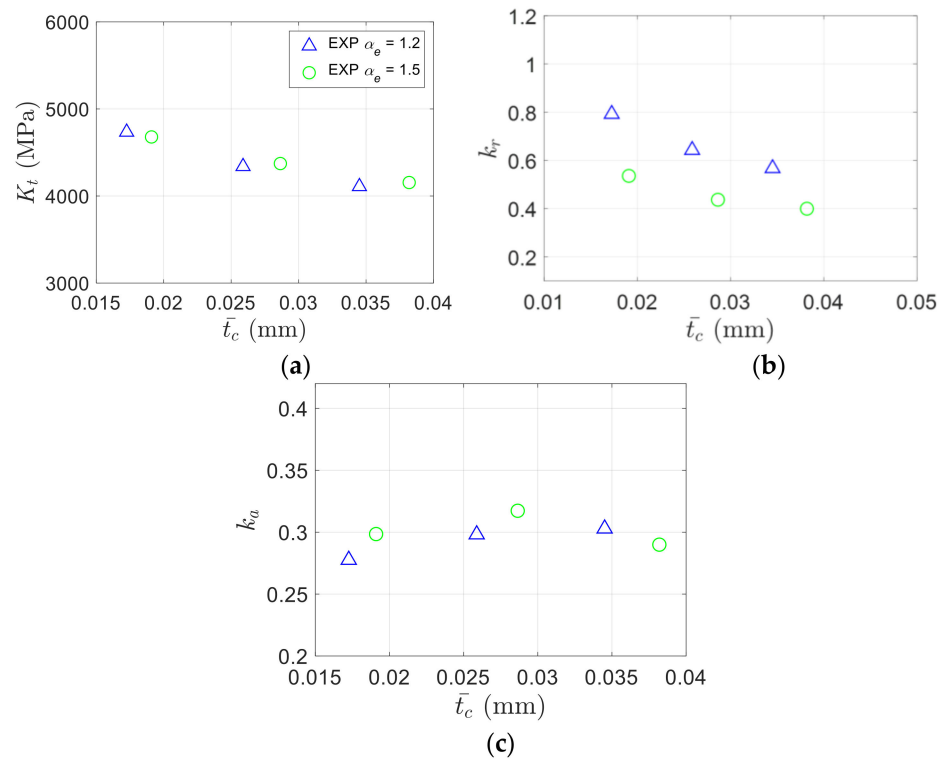


Figure 7. Experimental results for lumped cutting constants (LGCCs) as a function of average chip thickness. (a–c) are for the tangential, radial and axial cutting constants, respectively.

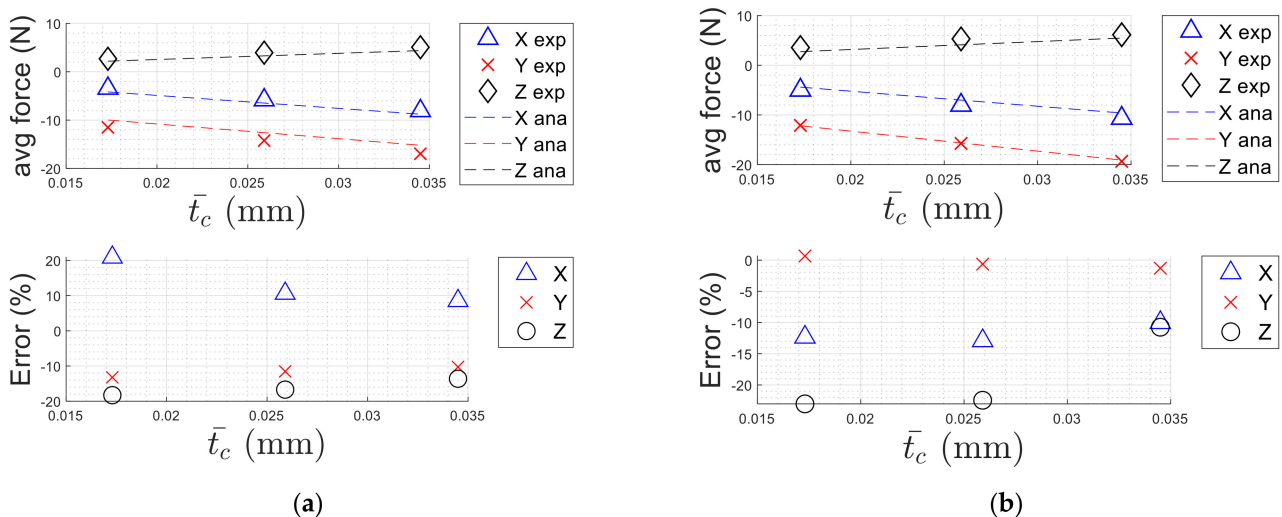


Figure 8. Experimental and predicted average side forces and percentage errors (a) for three sets of (ai, bi) at $a_e = 1.2$ mm, and (b) for three sets of (ci, di) at $a_e = 1.5$ mm.

Experimental data reported by DeMange et al. [46] for the high strain rate compression behavior of Inconel 718 under different heat treatment revealed that the aged and annealed 718 reached and was reaching, respectively, the same flow stress of approximately 2000 MPa at the strain range of 0.5 to 0.8 under various strain rates from 1681 to 4581. The extrapolated data suggest that materials from both heat treatments have nearly the same flow stress of 2000 MPa at the machining strain of 1.014 and strain rate of 22,270 for the presented experiment. Thus, the milling experimental results confirmed that, in combination with the presented oblique cutting mechanics, the J–C model for the aged 718 in [34] is also applicable for predicting the flow stress of annealed 718 in machining processes.

By using $T = T_{room}$ to calculate the shear low stress, the presented J–C model essentially disregards the explicit work material temperature softening effect represented by the material softening index, m , and it only considers the inherent thermal softening effect from plastic deformation in the shear plane, which was accounted for in the J–C parameters obtained from the SHPB experiment. The material softening term in Equation (5) could be ignored as in [49], but it can be retained for future work when modeling machining at elevated temperatures, such as in laser-assisted milling.

$T = T_{room}$ further assumes that the temperature rise on the machined surface from the preceding cut does not soften the work material for the subsequent cut. According to Equation (5), a temperature rise of 100 K for Inconel 718 reduces the flow stress by 3.66%. In the simulated orthogonal cutting of 718 in [34], the peak temperature rise on the machined surface was shown to be approximately 700 °C at 180 m/min for a cut depth of 0.1 mm using a tool with a zero rake angle and an edge radius of 16 µm. According to the 2D equation of heat conduction by Weiner [50] and experiments by Chu and Wallbank [51], this peak temperature rise can be demonstrated to reduce to less than 100 °C after 10 ms, which is the time interval between the consecutive cuts at 3000 rpm for a two-fluted end mill. The presented experiments further have a smaller uncut chip thickness with a smaller edge radius at a lower speed of $V_c = 56.5$ m/min; thus, a lower peak temperature rise than that in [34] should be expected to justify using $T = T_{room}$. However, as the milling speed increases, the temperature rise due to the previous cut might have to be considered for more accurate prediction of the cutting constants and milling forces.

More accurate in situ J–C model constants for Inconel 718 in milling could be estimated using the identified cutting constants and process variables presented in this paper. Recently, in-situ J–C model constants were identified through turning experiments by Ning et al. [52] for ultra-fine-grained titanium and by Ning and Liang [53] for AISI 1045 steel and Al6082-T6 aluminum.

4.4. Comparison with Published Experimental Results

The validity of the DGCC prediction model was verified by comparing the predicted results with those reported by Moufki et al. [29] for the milling force of Inconel 718 alloy. The workpiece material was a solution-treated and aged Inconel 718 alloy, with a hardness of 38 HRC. The milling tests were performed using an EPP-4120-05-T four-blade TiSiN coated end mill with a diameter of 12 mm, a helix angle of 43°, and a radial rake angle of 5°, which leads to a normal rake angle of $\alpha_n = 3.66^\circ$. In accordance with the milling conditions considered in [29], the axial depth of cut was set equal to $a_p = 8$ mm, the radial depth of cut $a_e = 1$ mm in down milling, and the feed per tooth was set as 0.07 mm with the bottom edge not engaged in the cutting. The experiments were performed in a nonlubricated condition using cutting speeds of 40, 60, and 80 m/min. The tool edge radius was not specified in [29]. Consequently, in implementing the presented DGCC model, the radius was assigned values of 0.005 mm and 0.01 mm, respectively, which are typical range of edge radii for this type of tool. Finally, the friction coefficient was taken from the paper to be 0.498, which is close to 0.485 for the presented experiments with different tool geometry and coating.

From this friction coefficient, the process variables and the six cutting constants can be found as presented in Sections 2.1 and 2.2. The normal friction angle from Equation (2) is $\beta_n = 26.47^\circ$, and the shear angle from Equation (1) has $\phi_n = 35.59^\circ$. The shear strain from Equation (3) and shear stress from Equation (5) are 2.08 and 1280.2 MPa at $V_c = 80$ m/min, respectively. Table 7 shows the predicted values of the six cutting constants for each of the tool edge radius and cutting speed conditions.

Table 7. Predicted shearing and ploughing constants.

| r_e (μm) | V_c (m/min) | K_{ts} (MPa) | k_{rs} | k_{as} | K_{te} (N/mm) | k_{re} | k_{ae} |
|-------------------------|---------------|----------------|----------|----------|-----------------|----------|----------|
| 5 μm | 40 | 4337.05 | 0.405 | 0.339 | 6.76 | 2.57 | 0 |
| | 60 | 4357.88 | 0.405 | 0.339 | 6.79 | 2.57 | 0 |
| | 80 | 4372.66 | 0.405 | 0.339 | 6.82 | 2.57 | 0 |
| 10 μm | 40 | 4337.05 | 0.405 | 0.339 | 13.52 | 2.57 | 0 |
| | 60 | 4357.88 | 0.405 | 0.339 | 13.59 | 2.57 | 0 |
| | 80 | 4372.66 | 0.405 | 0.339 | 13.63 | 2.57 | 0 |

In [29], the two ploughing constants were obtained from experiments to be $K_{te} = 19$ N/mm, $K_{re} = 39$ N/mm, or $k_{re} = 39/19 = 2.05$. The values of shearing coefficients were not given. For ploughing constants, the presented model predictions are $K_{te} = 6.8$ N/mm and $k_{re} = 2.57$ for an edge radius of 5 μm and $K_{te} = 13.6$ N/mm and $k_{re} = 2.57$ for an edge radius of 10 μm . These predicted values all fall within a reasonable range of the experimental results.

From the predicted cutting constants, the milling forces can be calculated using the convolution method presented in [20,21] or using the numerical integration approach in [29]. Figure 9 compares the corresponding results for the milling force with the experimental data reported in [29]. In general, both the results from [29] and the predicted cutting constants in Table 7 show that the cutting force and constants undergo no significant change as the cutting speed increases from 40 to 80 m/min. It can also be demonstrated that the shear flow stress increases by only about 1% if the thickness of the sheared element, Δy , in Equation (4) for strain rate is reduced from 25 to 10 μm . This can be expected due to the low strain rate sensitivity coefficient, $C = 0.0134$, in the adopted Johnson–Cook material law.

It is further revealed in Figure 9 that, under this cutting configuration, the change in edge ploughing forces from edge radii of 5 and 10 μm has a significant effect on the total milling force in the normal to feed direction, but little effect on the feed direction. This also demonstrates that the value and variation of the honed edge radius are important in the accurate prediction of milling forces. The milling force and its underlying ploughing constants can serve as effective quality indicators of a new or worn tool's cutting-edge condition.

The prediction errors can be calculated for the average and peak cutting forces in the X-, Y-, and Z-directions under the various cutting speeds and edge radii. For a smaller value of the tool edge radius (0.005 mm), the maximum deviation of the predicted force from the measured force is +10.23%/−20.81% for the average force and +10.5%/−17.74% for the peak force. For a larger tool edge radius of 0.01 mm, the maximum errors are +6.78%/−15.16% and +12.86%/−11.18% for the average and peak forces, respectively. In general, the milling forces predicted by the presented milling constants model agree well with the published experimental results.

In building the cutting constant prediction model from the identified friction angle, this paper adopted many existing models including the Merchant law, J–C model parameters, the orthogonal to oblique transformation for the cutting coefficients, and the edge ploughing force models. The effective combination of these existing equations and models with practical simplifying approximations provides a foundation for further investigation in the milling of Inconel 718 or other difficult-to-cut materials. For instance, this study and the work by Moufki et al. [29] both conducted experiments in dry condition. In reality, various types of coolants are applied in the industrial milling process. The presented model will facilitate investigation into the effects of coolant, coating, and edge preparation on the friction coefficient at the rake face, as well as on the shear flow stress with respect to various milling conditions, in future research and industrial applications.

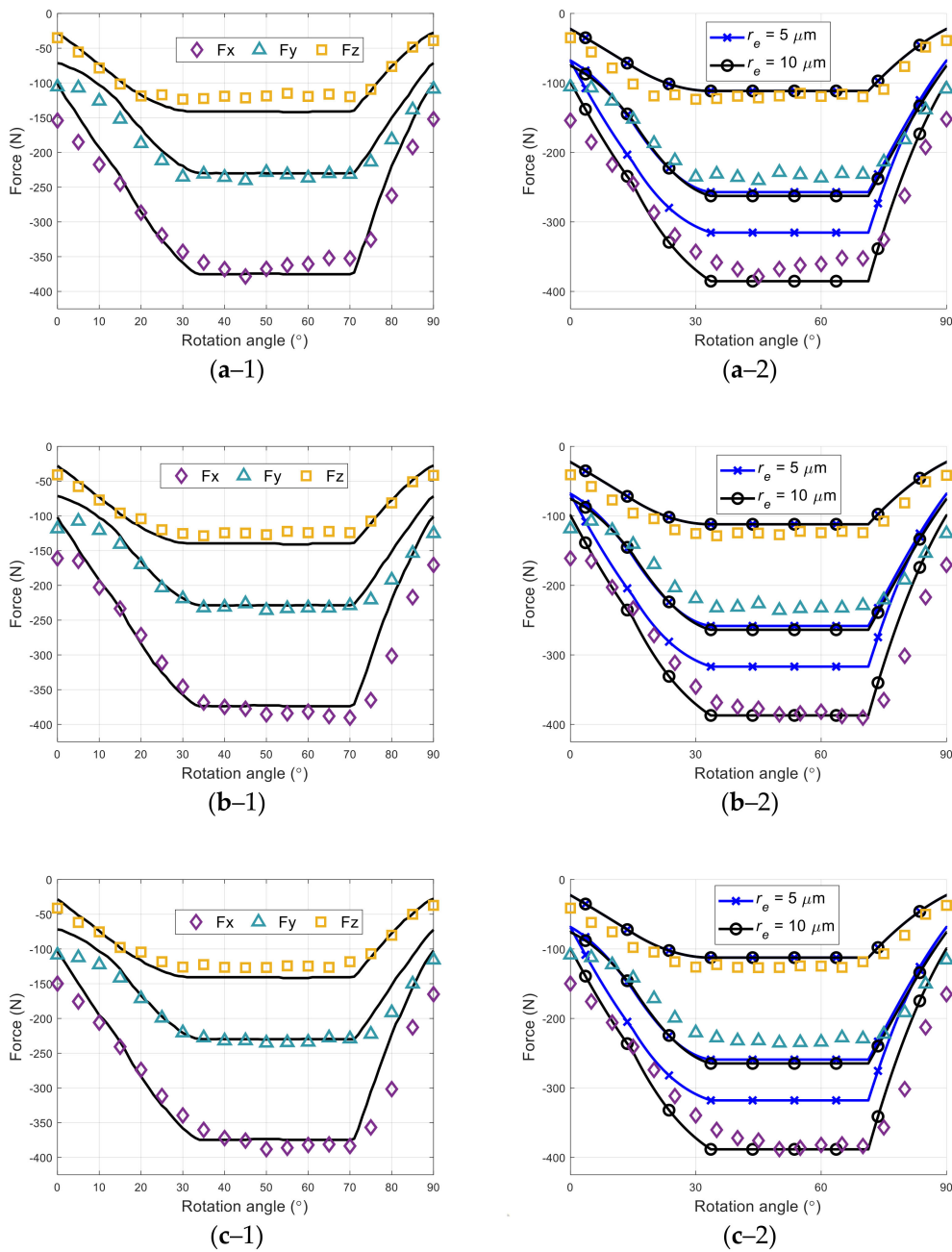


Figure 9. Comparison of predicted (lines) and experimental (symbols) milling forces. Note that figures (a–1), (b–1), and (c–1) refer to cutting speeds of 40, 60, and 80 m/min, respectively from [29], while figures (a–2), (b–2), and (c–2) refer to predictions by the presented model at two different tool edge radius values along with traced experimental forces. Note that forces in X- and Y-directions on the right are switched for direct comparison with results from [29].

5. Conclusions

This paper proposed an integrated dual-mechanism milling constant prediction model for Inconel 718 on the basis of orthogonal and oblique cutting theories, a material constitutive equation, and an explicit consideration of the tool edge ploughing mechanism. The experimental and predicted results support the following major conclusions:

1. The presented DGCC model requires the value of the normal mean friction angle or coefficient for a given combination of tool and work material. An identification formula was presented for the normal mean friction angle of oblique cutting in milling.

2. Within the recommended range of feed per tooth, the DGCC prediction results reveal that the shearing constants and edge ploughing constants remain approximately constant as the average chip thickness increases and are in good agreement with the experimentally identified cutting constants.
3. Both the predicted shearing constants using the classic Merchant's shear angle formula and the selected J–C material law and the predicted ploughing constants are reasonably within the experimental results. The predicted average values of the milling force by the predicted cutting constants are generally within $\pm 20\%$ of the experimental results.
4. The predicted forces from analytical cutting constants based on the reported friction coefficient and cutter geometry are within 20% and 15% of the average and peak forces, respectively, from published experimental results.
5. Without considering the thermal–mechanical coupling effect, the presented model is demonstrated to work well for milling of both annealed and aged Inconel 718 at cutting speeds of $V_c \leq 80$ m/min.

Author Contributions: Conceptualization, S.Y.L. and J.-J.J.W.; methodology, C.-J.L., S.Y.L. and J.-J.J.W.; software, C.-J.L. and J.-J.J.W.; validation, C.-J.L., Y.-F.L., H.-B.W. and J.-J.J.W.; formal analysis, C.-J.L. and J.-J.J.W.; investigation, all authors; resources, Y.-T.L. and J.-J.J.W.; data curation, C.-J.L., Y.-F.L., and H.-B.W.; writing—original draft preparation, C.-J.L. and J.-J.J.W.; writing—review and editing, S.Y.L. and J.-J.J.W.; visualization, C.-J.L. and J.-J.J.W.; supervision, J.-J.J.W.; project administration, Y.-T.L.; funding acquisition, Y.-T.L. and J.-J.J.W. All authors have read and agreed to the published version of the manuscript.

Funding: This work was partially supported by the Ministry of Science and Technology of Taiwan (Grant no: MOST 108-2622-E-006-022-CC3) and by the “Intelligent Manufacturing Research Center” (IMRC) from The Featured Areas Research Center Program within the framework of the Higher Education Sprout Project by the Ministry of Education (MOE) in Taiwan.

Data Availability Statement: Data are contained within the article.

Acknowledgments: The financial and equipment support provided to this study by the Metal Industries Research and Development Center (MIRDC) of Taiwan is greatly appreciated.

Conflicts of Interest: The authors declare no conflict of interest.

Abbreviations

| | |
|--|---|
| A, A_s, A_b | Average forces vectors for total, side, and bottom tool edges |
| a_e, a_p | Radial depth of cut and axial depth of cut |
| DGCC | Dual-mechanism global cutting constant |
| f_t, f_r | Local tangential force and radial force in milling |
| F_{ts}, F_{rs} | Tangential and radial chip shearing force of orthogonal cutting |
| F_t, F_r, F_a | Tangential, radial, and axial forces of oblique cutting |
| F_{te}, F_{re} | Tangential and radial edge ploughing forces |
| i | Tool helix angle |
| K_t, k_r, k_a | Cutting constants of LGCC model |
| $K_{ts}, k_{rs}, k_{as}, K_{te}, k_{re}, k_{ae}$ | Cutting constants of DGCC model |
| K_{ts_or}, k_{rs_or} | Tangential and radial shearing constants of orthogonal cutting |
| K_{te_or}, k_{re_or} | Tangential and radial ploughing constants of orthogonal cutting |
| LGCC | Lumped global cutting constant |
| N | Number of teeth |
| P | Average value of elementary cutting functions |
| r_e | Tool edge radius |
| R | Tool radius |
| \bar{t}_c | Average uncut chip thickness |
| t_0 | Uncut chip thickness |
| t_{min} | Minimum uncut chip thickness |

| | |
|----------------------|---|
| V_c | Cutting speed |
| w | Width of orthogonal cutting |
| α_n, α_r | Normal rake angle and radial rake angle |
| β_a, β_n | Mean and normal mean friction angle |
| γ | Shear strain |
| $\dot{\gamma}$ | Shear strain rate |
| δ | Feed per tooth |
| ε | Strain |
| $\dot{\varepsilon}$ | Strain rate |
| η_c | Chip flow angle |
| θ_1, θ_2 | Entry and exit angles |
| μ | Friction coefficient between chip and rake face |
| σ | Flow stress |
| τ | Shear flow stress |
| ϕ_n | Normal shear angle |

References

- Merchant, M.E. Mechanics of the Metal Cutting Process. I. Orthogonal Cutting and a Type 2 Chip. *J. Appl. Phys.* **1945**, *16*, 267–275. [[CrossRef](#)]
- Palmer, W.B.; Oxley, P.L.B. Mechanics of Orthogonal Machining. *Proc. Inst. Mech. Eng.* **1959**, *173*, 623–654. [[CrossRef](#)]
- Armarego, E.J.A.; Brown, R.H. *The Machining of Metals*; Prentice-Hall: Englewood Cliffs, NJ, USA, 1969.
- Stabler, G.V. The Fundamental Geometry of Cutting Tools. *Proc. Inst. Mech. Eng.* **1951**, *165*, 14–26. [[CrossRef](#)]
- Kobayashi, S.; Thomsen, E.G. Some Observations on the Shearing Process in Metal Cutting. *J. Eng. Ind.* **1959**, *81*, 251–262. [[CrossRef](#)]
- Albrecht, P. New Developments in the Theory of the Metal-Cutting Process: Part I. The Ploughing Process in Metal Cutting. *J. Eng. Ind.* **1960**, *82*, 348–357. [[CrossRef](#)]
- Waldorf, D.J.; Devor, R.E.; Kapoor, S.G. A Slip-Line Field for Ploughing During Orthogonal Cutting. *J. Manuf. Sci. Eng.* **1998**, *120*, 693–699. [[CrossRef](#)]
- Waldorf, D.J. A Simplified Model for Ploughing Forces in Turning. *J. Manuf. Process.* **2006**, *8*, 76–82. [[CrossRef](#)]
- Jun, M.B.G.; Liu, X.; Devor, R.E.; Kapoor, S.G. Investigation of the Dynamics of Microend Milling—Part I: Model Development. *J. Manuf. Sci. Eng.* **2006**, *128*, 893–900. [[CrossRef](#)]
- Malekian, M.; Park, S.S.; Jun, M.B. Modeling of dynamic micro-milling cutting forces. *Int. J. Mach. Tools Manuf.* **2009**, *49*, 586–598. [[CrossRef](#)]
- Park, S.; Malekian, M. Mechanistic modeling and accurate measurement of micro end milling forces. *CIRP Ann.* **2009**, *58*, 49–52. [[CrossRef](#)]
- Wojciechowski, S.; Matuszak, M.; Powalka, B.; Madajewski, M.; Maruda, R.; Krolczyk, G.M. Prediction of cutting forces during micro end milling considering chip thickness accumulation. *Int. J. Mach. Tools Manuf.* **2019**, *147*, 103466. [[CrossRef](#)]
- Jing, X.; Lv, R.; Chen, Y.; Tian, Y.; Li, H. Modelling and experimental analysis of the effects of run out, minimum chip thickness and elastic recovery on the cutting force in micro-end-milling. *Int. J. Mech. Sci.* **2020**, *176*, 105540. [[CrossRef](#)]
- Rahman, M.A.; Amrun, M.R.; SenthilKumarabc, A. Investigation of the critical cutting edge radius based on material hardness. *Int. J. Adv. Manuf. Technol.* **2016**, *88*, 3295–3306. [[CrossRef](#)]
- Rahman, M.A.; Rahman, M.; Kumar, A.S. Influence of cutting edge radius on small scale material removal at ultra-precise level. *Procedia CIRP* **2018**, *77*, 658–661. [[CrossRef](#)]
- Koenigsberger, F.; Sabberwal, A. An investigation into the cutting force pulsations during milling operations. *Int. J. Mach. Tool Des. Res.* **1961**, *1*, 15–33. [[CrossRef](#)]
- Kline, W.; Devor, R.; Lindberg, J. The prediction of cutting forces in end milling with application to cornering cuts. *Int. J. Mach. Tool Des. Res.* **1982**, *22*, 7–22. [[CrossRef](#)]
- Wang, J.-J.; Zheng, C. An analytical force model with shearing and ploughing mechanisms for end milling. *Int. J. Mach. Tools Manuf.* **2002**, *42*, 761–771. [[CrossRef](#)]
- Yellowley, I. Observations on the mean values of forces, torque and specific power in the peripheral milling process. *Int. J. Mach. Tool Des. Res.* **1985**, *25*, 337–346. [[CrossRef](#)]
- Wang, J.-J.; Liang, S.Y.; Book, W.J. Convolution Analysis of Milling Force Pulsation. *J. Eng. Ind.* **1994**, *116*, 17–25. [[CrossRef](#)]
- Zheng, L.; Chiou, Y.S.; Liang, S.Y. Three dimensional cutting force analysis in end milling. *Int. J. Mech. Sci.* **1996**, *38*, 259–269. [[CrossRef](#)]
- Wojciechowski, S.; Maruda, R.W.; Nieslony, P.; Królczyk, G.M. Investigation on the edge forces in ball end milling of inclined surfaces. *Int. J. Mech. Sci.* **2016**, *119*, 360–369. [[CrossRef](#)]
- Armarego, E.; Whitfield, R. Computer Based Modelling of Popular Machining Operations for Force and Power Prediction. *CIRP Ann.* **1985**, *34*, 65–69. [[CrossRef](#)]

24. Budak, E.; Altintas, Y.; Armarego, E.J.A. Prediction of Milling Force Coefficients From Orthogonal Cutting Data. *J. Manuf. Sci. Eng.* **1996**, *118*, 216–224. [\[CrossRef\]](#)
25. Gonzalo, O.; Jauregi, H.; Uriarte, L.G.; De Lacalle, L.N.L. Prediction of specific force coefficients from a FEM cutting model. *Int. J. Adv. Manuf. Technol.* **2008**, *43*, 348–356. [\[CrossRef\]](#)
26. Li, H.; Zhang, W.; Li, X. Modelling of cutting forces in helical end milling using a predictive machining theory. *Int. J. Mech. Sci.* **2001**, *43*, 1711–1730. [\[CrossRef\]](#)
27. Kobayashi, T.; Simons, J.W.; Brown, C.; Shockey, D. Plastic flow behavior of Inconel 718 under dynamic shear loads. *Int. J. Impact Eng.* **2008**, *35*, 389–396. [\[CrossRef\]](#)
28. Li, H.; Wang, J. A cutting forces model for milling Inconel 718 alloy based on a material constitutive law. *Proc. Inst. Mech. Eng. Part C J. Mech. Eng. Sci.* **2012**, *227*, 1761–1775. [\[CrossRef\]](#)
29. Moufki, A.; Le Coz, G.; Dudzinski, D. End-milling of Inconel 718 Superalloy—An Analytical Modelling. *Procedia CIRP* **2017**, *58*, 358–363. [\[CrossRef\]](#)
30. Uhlmann, E.; Von Der Schulenburg, M.G.; Zettier, R. Finite Element Modeling and Cutting Simulation of Inconel 718. *CIRP Ann.* **2007**, *56*, 61–64. [\[CrossRef\]](#)
31. Lu, X.; Wang, H.; Jia, Z.; Feng, Y.; Liang, S.Y. Coupled thermal and mechanical analyses of micro-milling Inconel 718. *Proc. Inst. Mech. Eng. Part B J. Eng. Manuf.* **2018**, *233*, 1112–1126. [\[CrossRef\]](#)
32. Long, Y.; Guo, C.; Ranganath, S.; Talarico, R.A. Multi-Phase FE Model for Machining Inconel 718. In Proceedings of the ASME 2010 International Manufacturing Science and Engineering Conference, Erie, PA, USA, 12–15 October 2010; Volume 1, pp. 263–269.
33. Ozel, T.; Llanos, I.; Soriano, J.; Arrazola, P. 3D Finite Element Modelling of Chip Formation Process for Machining Inconel 718: Comparison of Fe Software Predictions. *Mach. Sci. Technol.* **2011**, *15*, 21–46. [\[CrossRef\]](#)
34. Lorentzon, J.; Järvistråt, N.; Josefson, B. Modelling chip formation of alloy 718. *J. Mater. Process. Technol.* **2009**, *209*, 4645–4653. [\[CrossRef\]](#)
35. Pawade, R.; Sonawane, H.A.; Joshi, S.S. An analytical model to predict specific shear energy in high-speed turning of Inconel 718. *Int. J. Mach. Tools Manuf.* **2009**, *49*, 979–990. [\[CrossRef\]](#)
36. Ahmed, N.; Mitrofanov, A.; Babitsky, V.; Silberschmidt, V. Analysis of material response to ultrasonic vibration loading in turning Inconel 718. *Mater. Sci. Eng. A* **2006**, *424*, 318–325. [\[CrossRef\]](#)
37. Sonawane, H.A.; Joshi, S.S. Analytical modeling of chip geometry and cutting forces in helical ball end milling of superalloy Inconel 718. *CIRP J. Manuf. Sci. Technol.* **2010**, *3*, 204–217. [\[CrossRef\]](#)
38. Akmal, M.; Layegh, K.E.; Lazoglu, I.; Akgün, A. Yavaş, Çağlar Friction Coefficients on Surface Finish of AlTiN Coated Tools in the Milling of Ti6Al4V. *Procedia CIRP* **2017**, *58*, 596–600. [\[CrossRef\]](#)
39. Merchant, M.E. Mechanics of the Metal Cutting Process. II. Plasticity Conditions in Orthogonal Cutting. *J. Appl. Phys.* **1945**, *16*, 318–324. [\[CrossRef\]](#)
40. Merchant, M.; Zlatin, N. Nomographs for analysis of metal-cutting processes. *Mech. Eng.* **1945**, *67*, 737–742.
41. Shaw, M.C. *Metal Cutting Principles*; Oxford University Press: New York, NY, USA, 2005.
42. Johnson, G.R.; Cook, W.H. A Constitutive model and data for metals subjected to large strains, high strain rates and high temperatures. In Proceedings of the 7th International Symposium on Ballistics, The Hague, The Netherlands, 19–21 April 1983; Volume 21, pp. 541–547.
43. Altintas, Y. *Manufacturing Automation: Metal Cutting Mechanics, Machine Tool Vibrations, and CNC Design*; Cambridge University Press: New York, NY, USA, 2012.
44. Lee, E.H.; Shaffer, B.W. *Theory of Plasticity Applied to the Problem of Machining*; Division of Applied Mathematics: Brown Providence, RI, USA, 1949.
45. Grzesik, W.; Nieslony, P.; Laskowski, P. Determination of Material Constitutive Laws for Inconel 718 Superalloy Under Different Strain Rates and Working Temperatures. *J. Mater. Eng. Perform.* **2017**, *26*, 5705–5714. [\[CrossRef\]](#)
46. DeMange, J.J.; Pereira, J.M.; Lerch, B.A.; Prakash, V. Ballistic impact behavior of NI-based super alloys with applications to engine fan-blade containment. In Proceedings of the SEM IX International Congress on Experimental Mechanics, Orlando, FL, USA, 5–8 June 2000; pp. 44–47.
47. Pereira, J.; Lerch, B.A. Effects of heat treatment on the ballistic impact properties of Inconel 718 for jet engine fan containment applications. *Int. J. Impact Eng.* **2001**, *25*, 715–733. [\[CrossRef\]](#)
48. Lee, W.-S.; Lin, C.-F.; Chen, T.-H.; Chen, H.-W. Dynamic Impact Response of Inconel 718 Alloy under Low and High Temperatures. *Mater. Trans.* **2011**, *52*, 1734–1740. [\[CrossRef\]](#)
49. Mitrofanov, A.; Babitsky, V.; Silberschmidt, V.V. Thermomechanical finite element simulations of ultrasonically assisted turning. *Comput. Mater. Sci.* **2005**, *32*, 463–471. [\[CrossRef\]](#)
50. Weiner, J.H. Shear-Plane Temperature Distribution in Orthogonal Cutting. *Trans. ASME* **1955**, *77*, 1331–1341.
51. Chu, T.H.; Wallbank, J. Determination of the Temperature of a Machined Surface. *J. Manuf. Sci. Eng.* **1998**, *120*, 259–263. [\[CrossRef\]](#)
52. Ning, J.; Nguyen, V.; Huang, Y.; Hartwig, K.T.; Liang, S.Y. Inverse determination of Johnson–Cook model constants of ultra-fine-grained titanium based on chip formation model and iterative gradient search. *Int. J. Adv. Manuf. Technol.* **2018**, *99*, 1131–1140. [\[CrossRef\]](#)
53. Ning, J.; Liang, S.Y. Inverse identification of Johnson–Cook material constants based on modified chip formation model and iterative gradient search using temperature and force measurements. *Int. J. Adv. Manuf. Technol.* **2019**, *102*, 2865–2876. [\[CrossRef\]](#)